Spin waves and Dirac magnons in a honeycomb-lattice zigzag antiferromagnet BaNi$_2$(AsO$_4$)$_2$

Bin Gao [1,*] Tong Chen,[1,*] Chong Wang,[2] Lebing Chen [1] Ruidan Zhong,[3]
Douglas L. Abernathy [4] Di Xiao,[2,†] and Pengcheng Dai [1,‡]

[1]*Department of Physics and Astronomy, Rice University, Houston, Texas 77005, USA*
[2]*Department of Physics, Carnegie Mellon University, Pittsburgh, Pennsylvania 15213, USA*
[3]*Tsung-Dao Lee Institute and School of Physics and Astronomy, Shanghai Jiao Tong University, Shanghai 200240, China*
[4]*Neutron Scattering Division, Oak Ridge National Laboratory, Oak Ridge, Tennessee 37831, USA*

The topological properties of massive and massless fermionic quasiparticles have been intensively investigated over the past decade in topological materials without magnetism. Recently, the bosonic analogs of such quasiparticles arising from spin waves have been reported in a two-dimensional (2D) honeycomb-lattice ferromagnet/antiferromagnet and a 3D antiferromagnet. Here, we use time-of-flight inelastic neutron scattering to study spin waves of the $S = 1$ honeycomb-lattice antiferromagnet BaNi$_2$(AsO$_4$)$_2$, which has a zigzag antiferromagnetic (AFM) ground state identical to that of the Kitaev quantum spin liquid candidate α-RuCl$_3$. We determine the magnetic exchange interactions in the zigzag AFM ordered phase, and show that spin waves in BaNi$_2$(AsO$_4$)$_2$ have symmetry-protected Dirac points inside the Brillouin zone boundary. These results provide a microscopic understanding of the zigzag AFM order and associated Dirac magnons in honeycomb-lattice magnets, and are also important for establishing the magnetic interactions in Kitaev quantum spin liquid candidates.

I. INTRODUCTION

Elucidating nontrivial crossing points in the band structure of a crystalline solid plays an important role in understanding its momentum space topology [1–3]. The discovery of massless Dirac fermions in the electron bands of graphene has led to intensive studies of topological phases in metallic systems [4,5]. A plethora of topologically nontrivial electron band structures with massless and massive fermionic quasiparticles have been proposed and studied in electronic systems [6,7]. However, band topology is not restricted to fermionic systems and can also be extended to bosonic quasiparticles [8–22]. In magnetic ordered materials where spin waves are bosons, topological bosonic quasiparticles (magnons) are characterized by chiral edge states and a spin gap at the Dirac points induced by the next-nearest-neighbor Dzyaloshinskii-Moriya (DM) interaction, as found in the two-dimensional (2D) honeycomb ferromagnet CrI$_3$/CrBr$_3$/CrGeTe$_3$ [14–17], or symmetry-protected band crossings, such as the magnon Dirac cones in the 3D antiferromagnet Cu$_3$TeO$_6$ [18,19] and the 2D honeycomb-lattice antiferromagnet CoTiO$_3$ [20]. Recently, the topological properties of magnon bands in collinear magnetic orders have been investigated on the honeycomb lattice. While the ferromagnetic (FM) phase exhibits a magnon spectrum similar to the electron dispersion of graphene, the antiferromagnetic (AFM)

phases show an even richer magnon structure. In particular, the zigzag AFM ordered phase, shown in Figs. 1(a) and 1(b), can host a Dirac nodal line protected by nonsymmorphic symmetry combined with time-reversal symmetry [21,22].

In addition to potentially hosting topological magnon bands, 2D honeycomb-lattice magnetic materials themselves are of great interest because the Kitaev spin model [23], consisting of a network of spins with $S = 1/2$ on a honeycomb lattice, is predicted to host a quantum spin liquid (QSL) with Majorana fermions as its excitations, important for quantum computation [24]. Although there is no confirmed Kitaev QSL material, α-RuCl$_3$ has been identified as a candidate with a zigzag AFM ground state [Fig. 1(b)] [25]. One unsolved quest is to determine magnetic exchange couplings giving rise to the zigzag AFM order, which is necessary to extract Kitaev interactions in α-RuCl$_3$ [26]. Actually, this quest has not been completely solved in all 2D honeycomb-lattice magnets with a zigzag AFM ground state, despite many compounds having been studied [27–33]. Inelastic neutron scattering (INS) experiments carried out on powder samples of some of these compounds provided constraints on the magnetic exchange couplings [31,34,35]. Nevertheless, no measurements on single crystals have conclusively unveiled the magnetic couplings giving rise to the zigzag AFM structure.

BaNi$_2$(AsO$_4$)$_2$ is a rare example of a 2D honeycomb-lattice magnet with $S = 1$ and a zigzag AFM structure [Figs. 1(a) and 1(b)] [36], in which magnetic exchange couplings could be completely determined. Unfortunately, early INS experiments carried out on single crystals of BaNi$_2$(AsO$_4$)$_2$ and related compounds [37–40] have not mapped out the entire spin wave spectra, due to limitation of the spectrometers used
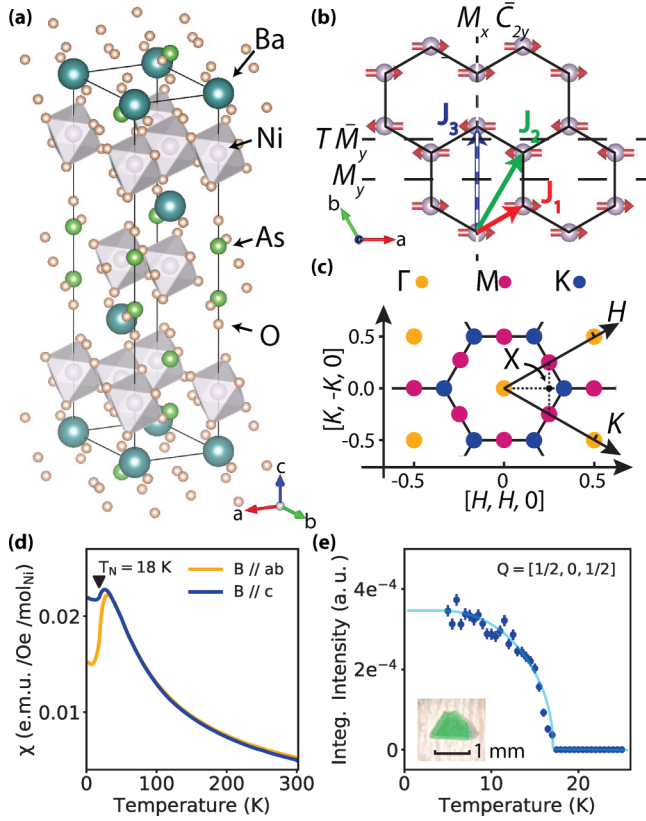

FIG. 1. (a) Crystal structure of $BaNi_2(AsO_4)_2$. (b) Top-down view of the nickel honeycomb lattice with Heisenberg exchange paths. (c) The Brillouin zone boundaries and high-symmetry points in the $[H, K]$ plane. (d) Susceptibility of $BaNi_2(AsO_4)_2$ measured with a 1 T magnetic field applied parallel to the c axis and ab plane. The sharp turn in susceptibility data indicates a magnetic phase transition at $T_N = 18$ K. (e) Order-parameter-like $(1/2, 0, 1/2)$ magnetic Bragg peak. Inset: Photograph of the single crystal used in the susceptibility measurement.

nearly four decades ago. In addition, the isostructural compound $BaCo_2(AsO_4)_2$, which has a helical magnetic ground state at zero field [41], has been recently proposed as a candidate for a field-induced Kitaev QSL state [42]. Therefore, it is of great interest to map out spin waves in $BaNi_2(AsO_4)_2$ and determine the magnetic exchange couplings and topological properties.

In this paper, we report INS studies of spin waves on single crystals of $BaNi_2(AsO_4)_2$. Using neutron time-of-flight spectroscopy, we map out spin waves in the AFM ordered state and fit the data with a Heisenberg Hamiltonian to determine the magnetic exchange couplings. The spectra reveal signatures of Dirac points around the high-symmetry point X in the 2D Brillouin zone. Our symmetry analysis and calculation based on linear spin wave theory show that the Dirac point is due to the coexistence of easy-axis and easy-plane anisotropy, and is protected by symmetry. On warming to temperatures above T_N, spin waves in the ordered state become broader but still have short-range in-plane spin correlations that decay with increasing temperature. Our results therefore determine the magnetic exchange couplings of a zigzag AF honeycomb-

lattice magnet, and provide a basis to compare with theoretical calculations using a Heisenberg-Kitaev Hamiltonian.

II. EXPERIMENT

$BaNi_2(AsO_4)_2$ crystallizes in a tetragonal structure with the in-plane and c-axis lattice parameters $a = 4.94$ Å and $c = 23.43$ Å, respectively (space group $R\bar{3}$) [Fig. 1(a)]. Octahedrally coordinated Ni^{2+} ions form a 2D honeycomb network, separated by AsO_4-Ba-AsO_4 layers [Fig. 1(b)]. The compound has an ABC stacking along the c axis. The distance between nearest-neighbor Ni^{2+} ions is 2.85 Å, while the interlayer distance is 7.89 Å, making an ideal 2D magnetic honeycomb lattice. Upon cooling, the system orders antiferromagnetically below $T_N \approx 18$ K with Ni^{2+} spins forming zigzag chains parallel or antiparallel to the a axis [Fig. 1(b)] [36]. Figure 1(c) shows a schematic of the reciprocal space in which the momentum transfer $Q = Ha^* + Kb^* + Lc^*$ is denoted as (H, K, L) reciprocal lattice units (r.l.u.). The zigzag AFM transition at $T_N \approx 18$ K is confirmed by magnetic susceptibility [Fig. 1(d)] and neutron diffraction measurements [Fig. 1(e)].

The polycrystalline sample was synthesized using a solid state method. Stoichiometric powders of BaO (99.9%, Alfa Aesar), NiO (99.9%, Alfa Aesar), and As_2O_5 (99.9%, Alfa Aesar) were mixed, pressed, and sintered at 850 °C in an evacuated quartz tube. Plate-shaped single crystals of $BaNi_2(AsO_4)_2$ was grown by using NaCl as the flux with a molar ratio of 1:50. Green transparent crystals [Fig. 1(e) inset] with a typical size of $1 \times 1 \times 0.2$ mm and clear hexagonal edges were separated from the flux by dissolving in hot water.

We coaligned more than 100 pieces of single crystals with a total mass of $\sim$1.5 g in the $[H, K, 0]$ scattering plane and carried out time-of-flight inelastic neutron scattering experiments using the ARCS Spectrometer, Spallation Neutron Source, Oak Ridge National Laboratory. We used an incident neutron energy of $E_i = 16$ meV with a high-resolution mode to do rotational scans at 6, 17, 20, 37, and 80 K.

III. RESULTS AND DISCUSSION

The left panels in Figs. 2(a)–2(d) show measured **Q**-E spectra of spin waves along high-symmetry directions within the $[H, K]$ plane at $T = 6$ K. The left panels in Figs. 2(e)–2(h) are the **Q** dependences of spin waves in the $[H, K]$ plane at energies $E = 2 \pm 0.5$, 3 ± 0.5, 4 ± 0.5, and 6 ± 0.5 meV, respectively. The measured intensities below the line plots (white lines) between the K and Γ points in Figs. 2(a) and 2(d) are due to the finite integration range perpendicular to the cutting direction $(-0.1 \leqslant K_\perp \leqslant 0.1)$. The spin wave spectra consist of four branches, consistent with the zigzag AFM structure that has four Ni^{2+} ions in the magnetic unit cell within the 2D plane. For magnetic ordered systems, the ordered moment direction is typically determined by dipolar interactions or single-ion anisotropy associated with spin-orbit coupling (SOC), where both can induce a spin gap at the ordering wave vector [43]. The size of the spin gap indicates the finite energy cost for the spins to fluctuate away from the ordered direction. The presence of the spin gaps at the M points [Figs. 2(a)–2(c)], especially the double-gap modes in
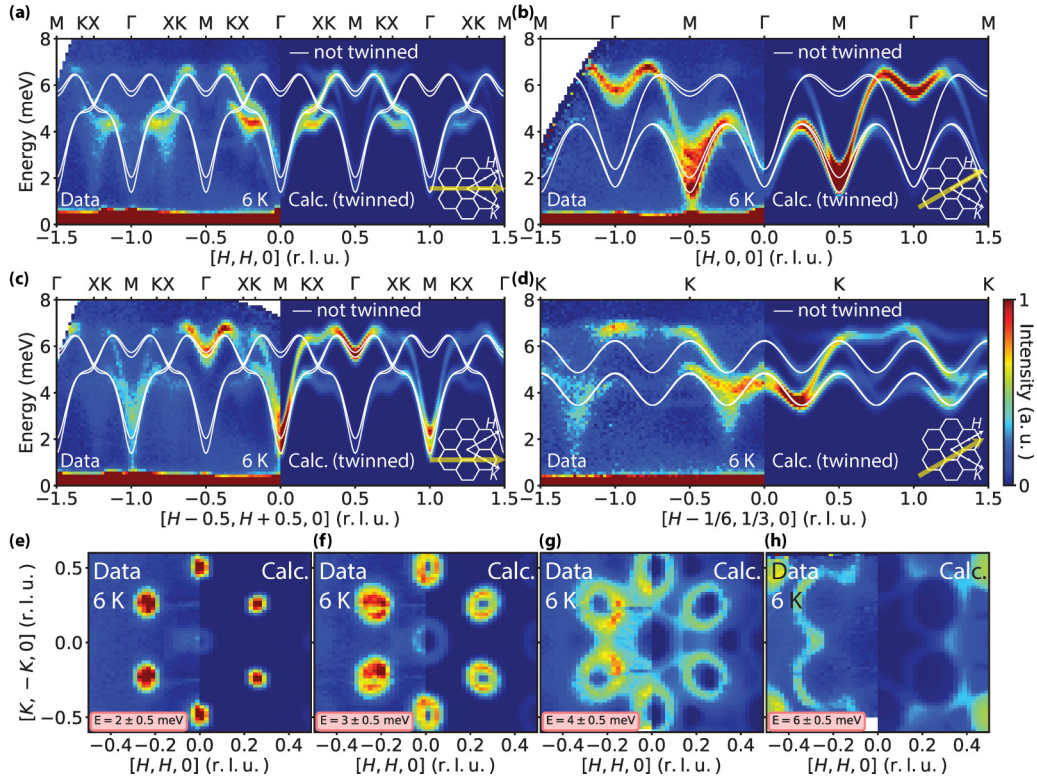
FIG. 2. (a)–(d) Neutron scattering E-$\mathbf{Q}$ spectra along high-symmetry directions experimentally at 6 K (left), compared with the calculated intensities and dispersion (twinned) discussed in the text (right). The line plots of a selected domain (not twinned) were overplotted on the measured and calculated dispersion. The experimental data were integrated over $-4 \leqslant L \leqslant 4$ and $-0.1 \leqslant K_{\perp} \leqslant 0.1$. (e)–(h) Constant-energy cuts at selected energy transfers in the $[H, K]$ plane at 6 K compared with the calculated pattern. The experimental data were integrated over $-4 \leqslant L \leqslant 4$.

Figs. 2(b) and 2(c), reveals that both easy-plane and easy-axis anisotropies should be taken into account to understand the spin waves of $BaNi_2(AsO_4)_2$.

In order to determine the magnetic exchange couplings in $BaNi_2(AsO_4)_2$, we compared the measured spin waves with the spectra calculated using the linear spin wave theory via the SPINW program [44]. We assumed a general Hamiltonian

$$H = \sum_{i<j}(J_1\mathbf{S}_i \cdot \mathbf{S}_j + J_2\mathbf{S}_i \cdot \mathbf{S}_j + J_3\mathbf{S}_i \cdot \mathbf{S}_j)$$
$$+ \sum_j D_z(S_j^z)^2 + \sum_j D_x(S_j^x)^2, \qquad (1)$$

where J_1, J_2, and J_3 are nearest-, next-nearest-, and next-next-nearest-neighbor coupling constants [Fig. 1(b)], and the D_z and D_x terms in the equation describe the easy-plane and easy-axis anisotropies of the Ni^{2+} ions, respectively. The overall Hamiltonian is similar to the ones used to describe the similar compounds $BaNi_2(PO_4)_2$ and $BaNi_2(VO_4)_2$, where single-ion anisotropies are introduced [36,38]. We do not consider in-plane anisotropic interactions (Kitaev term) due to the small SOC for Ni^{2+} ions in an octahedral local configuration [24,45]. Interlayer magnetic exchange couplings were also not included because there was no evidence of spin wave modulation along the L direction, suggesting negligible c-axis magnetic exchange coupling.

Since $BaNi_2(AsO_4)_2$ has zigzag AFM order, spin waves stem from the M point where there is a strong magnetic Bragg peak [Figs. 2(b) and 2(c)]. To fit the spin wave spectra, we set the signs of the initial magnetic exchange interactions to be consistent with the zigzag magnetic order. Then the exchange parameters were varied manually to compare the simulated spectra with the experimental data. The best fit yields $J_1 = -0.69$, $J_2 = -0.03$, $J_3 = 1.51$, $D_z = 0.15$, and $D_x = -0.12$ meV [the right panels in Figs. 2(a)–2(h)]. These results are compatible with the susceptibility measurement [Fig. 1(d)] through the relation $\Theta_{CW} = -S(S + 1)(g - 1)^2\Sigma_{i=n,nn,nnn}z_iJ_i/3k_B$, where $S = 1$ is the spin value, k_B is the Boltzmann constant, g is the Landé factor, and z_i is the number of neighbors coupled to each magnetic ion by the magnetic exchange J_i [34,46]. We note that the exchange couplings extracted from our measured spin waves are different from previous reports [36]. In spin wave dispersion along the $[H, H, 0]$, $[H, 0, 0]$, $[H - 0.5, H + 0.5, 0]$, and $[H - 1/6, 1/3, 0]$ directions [Figs. 2(a)–2(d)], and constant-energy cuts with different energies [Figs. 2(e)–2(h)], the calculations describe the measured data quite well. In particular, the anisotropy terms D_z and D_x reproduced the observed double-gap modes in the dispersion along the $[H, 0, 0]$, and $[H - 0.5, H + 0.5, 0]$ directions [Figs. 2(b) and 2(c)].

The magnetic interaction of $BaNi_2(AsO_4)_2$ can be described by the Hamiltonian in Eq. (1). From the fitting above, we got $D_z > 0$ and $D_x < 0$, describing the easy-plane and
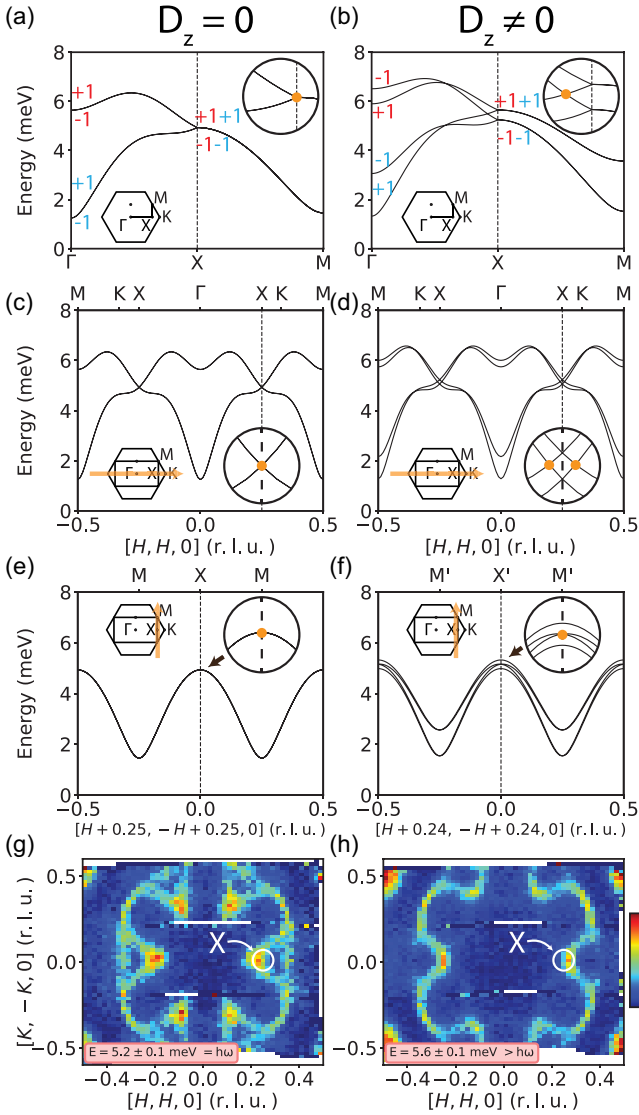
FIG. 3. (a), (b) Line plots of spin wave dispersion along high-symmetry directions with $D_z = 0$ (a) and 0.5 meV (b). The signs of the M_y eigenvalues were labeled. (c), (d) Calculated line plot of spin wave dispersion (not twinned) along the $[H, H, 0]$ direction with $D_z = 0$ (c) and 0.2 meV (d). (e), (f) Calculated line plot of spin wave dispersion (not twinned) along the perpendicular direction across the Dirac points in (c) and (d). (g), (h) Constant-energy cuts at selected energy transfers in the $[H, K]$ plane at 6 K. The experimental data were integrated over $-4 \leqslant L \leqslant 4$.

easy-axis anisotropies of the Ni^{2+} ions, respectively. Here, from symmetry arguments, we interpret the magnon dispersion of the above Hamiltonian, and establish the existence of topological Dirac points and nodal lines.

With the zigzag AFM ordering, the system respects M_x, M_y, $\bar{C}_{2y} = t(a_2)C_{2y}$, $\bar{M}_z = t(a_2)M_z$, and $T\bar{M}_y = Tt(a_1/2)M_y$ [Fig. 1(b)]. Here, $a_1 = (1, 0)$ and $a_2 = (1/2, \sqrt{3}/2)$ are the two lattice vectors (without the magnetic order). We will start the discussion from a simplified $D_z = 0$ case, where the $S_x = \sum_i S_i^x$ is a conserved quantity. The magnon bands with $D_z = 0$ are presented in Fig. 3(a). Along the X-M line, every band is fourfold degenerate, which splits into two doubly degenerate

bands on the Γ-X line. On the X-M line, $(T\bar{M}_y)^2 = -1$, indicating a Kramers degeneracy. On the other hand, $T\bar{M}_y$ commutes with S_x, indicating the Kramers pair is within the same eigenspace of S_x. In addition, $\bar{C}_{2y}$ anticommutes with S_x, forcing different eigenspaces of S_x to be degenerate, leading to the observed fourfold degeneracy. The doubly degeneracy on the Γ-X line is protected by the anticommuting operators $M_y S_x = -S_x M_y$ or $\bar{M}_z S_x = -S_x \bar{M}_z$, meaning the two magnons in the doubly degenerate band belong to separate eigenspaces of M_y or $\bar{M}_z$.

For finite D_z, S_x is no longer a good quantum number. Therefore, the doubly degeneracy on the Γ-X line is lifted. Especially, the crossings between the originally two degenerate bands [Fig. 3(b)] are protected by M_y or $\bar{M}_z$. These crossings are actually nodal lines since $\bar{M}_z$ is respected in the whole Brillouin zone. Besides the crossings within the originally degenerate bands, there is another crossing labelled by yellow dot [Fig. 3(b)], which we will argue is inevitable for small D_z. Especially, we will argue that the four degenerate bands (with $D_z = 0$) at X are split into two degenerate states with M_y eigenvalues $\{+1, +1\}$ and $\{-1, -1\}$ [Figs. 3(c)–3(f)]. To show this, we need to use the following three commutation relations that hold at X: $M_x M_y = M_y M_x$, $M_y \bar{C}_{2y} = \bar{C}_{2y} M_y$, and $M_x \bar{C}_{2y} = -\bar{C}_{2y} M_x$. We now use proof by contradiction and assume every doubly degenerate band at the X point has states $\{\varphi_{+1}, \varphi_{-1}\}$ with M_y eigenvalues $\{+1, -1\}$. Since M_x commutes with M_y, $M_x \varphi_{+1}$ should also be an M_y eigenstate with $+1$ eigenvalue. Therefore, $M_x \varphi_{+1} \propto \varphi_{+1}$, which means φ_{+1} is also an eigenstate of M_x with eigenvalue λ. Furthermore, since M_x anticommutes with $\bar{C}_{2y}$, $\bar{C}_{2y}\varphi_{+1}$ should be an eigenstate of M_x with eigenvalue $-\lambda$. As a result, $\bar{C}_{2y}\varphi_{+1} \propto \varphi_{-1}$. Finally, M_y commutes with $\bar{C}_{2y}$, indicating $\bar{C}_{2y}\varphi_{+1} \propto \varphi_{-1}$ is an eigenstate of M_y with eigenvalue $+1$. This contradicts the original assumption that φ_{-1} is an eigenstate of M_y with eigenvalue -1. Therefore, every doubly degenerate band at X has M_y eigenvalues $\{+1, +1\}$ or $\{-1, -1\}$. With the knowledge of the M_y eigenvalues on the Γ-X line and at the X points, it is evident that the crossing labelled by yellow dot is unavoidable, which is a topological Dirac point [Figs. 3(c)–3(f)].

To compare the above discussion with the data, we show constant-energy cuts at [Fig. 3(g)] and slightly above [Fig. 3(h)] the energy $E = 5.2$ meV where we expect Dirac crossings. Although twinned domains and finite energy resolution give rise to complicated features in the constant-energy cuts, we can clearly see the maxima of intensity are around the X points as marked in Figs. 3(g) and 3(h), which provides direct evidence of the existence of the Dirac points in the spectrum.

In strongly correlated electron materials such as the parent compound of iron-based superconductors, in-plane spin-spin correlations are weakly dependent on the AFM ordering temperatures of the system [47]. To test if this is also the case for zigzag ordered $BaNi_2(AsO_4)_2$, we show in Fig. 4 the temperature dependence of the constant-energy cuts at $T = T_N - 1.5 = 17$ K and $T = T_N + 18.5 = 37$ K with energies of $E = 0, 2, 3, 4, 5, 6$ meV. In the elastic channel, magnetic ordered peaks at the M points below T_N disappear at 37 K [Fig. 4(a)]. However, with finite energy transfer [Figs. 4(b)–
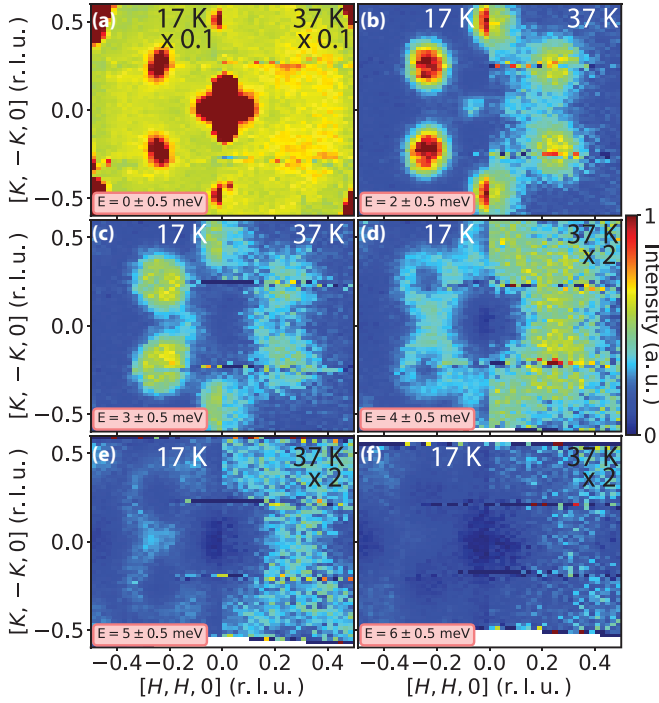
FIG. 4. (a)–(e) Temperature dependence of constant-energy cuts at selected energy transfers in the $[H, K]$ plane. The data were integrated over $-4 \leqslant L \leqslant 4$. The elastic scattering in (a) and the inelastic scattering at 37 K showed in the right panels of (d)–(f) were multiplied by 0.1 and 2, respectively. We see clear spin correlations at $T = 37 \approx 2T_N$ K.

4(f)], although intensities dramatically drop upon warming, the spin correlations persist up to 37 K.

By normalizing the observed magnetic scattering $S(\mathbf{Q}, E)$ with a vanadium standard, we can estimate the imaginary part of the dynamic susceptibility $\chi''(\mathbf{Q}, E)$ in absolute units via $\chi''(\mathbf{Q}, E) = [1 - \exp(-E/k_B T)]S(\mathbf{Q}, E)$, where k_B is the Boltzmann constant. The data points in Fig. 5(a) show the estimated energy dependence of the local dynamic susceptibility $\chi''(E) = \int \chi''(\mathbf{Q}, E)d\mathbf{Q} / \int d\mathbf{Q}$, where the integration is within the first Brillouin zone [48]. Calculations using a Heisenberg Hamiltonian assuming $S = 1$ shown in the dashed and solid lines are comparable to the observation, thus confirming that the $S = 1$ Heisenberg Hamiltonian can describe the data. In correlated electron materials such as the parent compound of iron-based superconductors, in-plane spin-spin correlations are weakly dependent on the AFM ordering temperature of the system [47]. To test if this is also the case for zigzag ordered $BaNi_2(AsO_4)_2$, we show in Figs. 5(b)–5(d) the temperature dependence of the spin wave dispersion along the $[H, 0, 0]$ direction. In the elastic channel, magnetic ordered peaks at the M points disappear above T_N [Fig. 1(e)]. However, with finite energy transfer [Figs. 5(b)–5(d)], the in-plane spin-spin correlations persist up to even 80 K, consistent with the 2D nature of the magnetic scattering [49].

To compare magnetic exchange couplings of the zigzag ordered $BaNi_2(AsO_4)_2$ with related compounds $BaNi_2(PO_4)_2$ and $BaNi_2(VO_4)_2$, we note that the latter compounds have different magnetic structures. The local moments on each Ni site in $BaNi_2(PO_4)_2$ and $BaNi_2(VO_4)_2$ are antiparal-

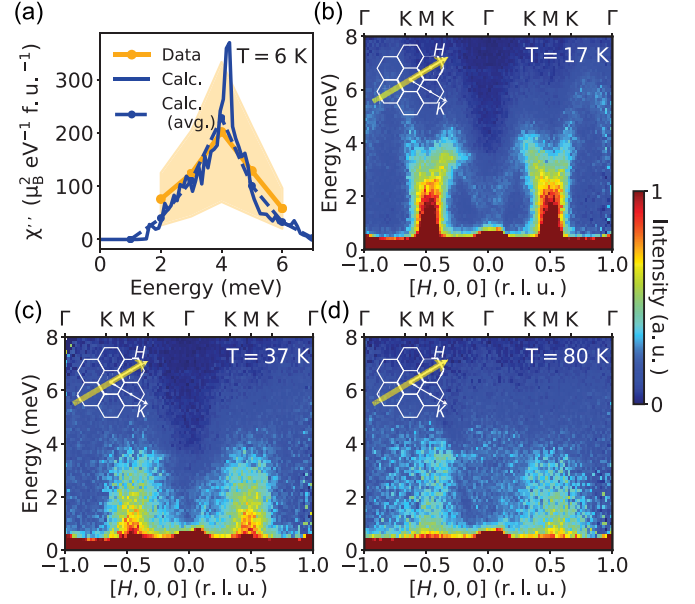FIG. 5. (a) Measured (orange) and calculated (blue) energy-dependent local dynamic susceptibilities of $BaNi_2(AsO_4)_2$, obtained by integration in the first Brillouin zone in the $[H, K]$ plane. The light orange region indicates the uncertainty of the experiment data mainly from the normalization process. Calculated local dynamic susceptibility averaged every meV is also plotted to directly compare with measured data. (b)–(d) Temperature dependence of neutron scattering E-$\mathbf{Q}$ spectra along the $[H, 0, 0]$ direction observed at 17, 37, and 80 K. The experimental data were integrated over $-4 \leqslant L \leqslant 4$ and $-0.1 \leqslant K_\perp \leqslant 0.1$.

lel to each other, and the direction of the moments in $BaNi_2(PO_4)_2$ is along the bond. Table I summarizes the nearest, second-nearest, third-nearest magnetic exchange couplings, easy-plane and easy-axis anisotropy, and Kitaev and Γ terms in $BaNi_2(XO_4)_2$ (X = V, P, As) and α-$RuCl_3$.

As we can see from the table, the magnetic structure and properties are very sensitive to exchange couplings in an AFM honeycomb-lattice magnet. In previous neutron scattering work on single crystals of $BaM_2(XO_4)_2$ (M = Ni, Co; X = V, P, As), spin wave spectra were only measured along selected high-symmetry directions with poor resolution using a triple-axis neutron spectrometer [37–41], much different from the entire spin wave spectra obtained using a high-resolution neutron time-of-flight chopper spectrometer (Figs. 2–4) [50].

TABLE I. The estimated magnetic interactions and anisotropies in $BaNi_2(XO_4)_2$ (X = V, P, As) [36,38] and α-$RuCl_3$ [52,53] from representative studies. All units are converted to meV.

	$BaNi_2As_2O_8$	$BaNi_2V_2O_8$	$BaNi_2P_2O_8$	α-$RuCl_3$	α-$RuCl_3$
J_1	-0.69	12.3	0.19	-1.53	-0.35
J_2	-0.03	1.25	0.025		
J_3	1.51	0.2	0.76		0.34
D_z	0.15	0.07	0.269		
D_x	-0.12	-0.001			
K				-6.55	5.25
Γ				-2.8	2.4

The J_1, J_2, and J_3 parameters determined in our experiment for $BaNi_2(AsO_4)_2$ are consistent with the proposed phase diagram for an $S = 1$ zigzag ordered antiferromagnet in a classical Heisenberg Hamiltonian [21,51].

The evolution of magnetic Dirac bosons in the honeycomb lattice has been calculated before in two papers. Several AFM structures have been discussed, including simple AFM, zigzag, dimerized, armchair, and stripe. In the simple AFM structure, the breaking of inversion symmetry eliminates the presence of a Dirac point, while in more complex AFM configurations, the crossing of spin waves can produce Dirac-like nodes. However, there is no experimental confirmation from any real materials of a complex AFM structure. In the case of $CoTiO_3$, it is actually a FM correlation in the 2D honeycomb lattice. Also notice that the Dirac points in $BaNi_2(AsO_4)_2$ are not on the boundary of the Brillouin zone, not as in the case of a 2D FM honeycomb lattice $CoTiO_3$ nor the 3D antiferromagnet Cu_3TeO_6 [18,19]. This is due to the more generalized magnetic structure in $BaNi_2(AsO_4)_2$, which has lower symmetry.

IV. CONCLUSIONS

In summary, we used time-of-flight inelastic neutron scattering to study spin waves of the $S = 1$ honeycomb-lattice antiferromagnet $BaNi_2(AsO_4)_2$, which has a zigzag AFM ground state. We determine the magnetic exchange interactions in the zigzag AFM ordered phase, and show that spin waves in $BaNi_2(AsO_4)_2$ have symmetry-protected Dirac points inside the Brillouin zone boundary. These results provide a microscopic understanding of the zigzag AFM order and associated Dirac magnons in honeycomb-lattice magnets, and are also important for establishing the magnetic interactions in Kitaev quantum spin liquid candidates.

APPENDIX

Here, we present a detailed symmetry analysis of the magnon band structure. In the main text, we have argued that the bands on the Γ-X are doubly degenerate with $\{+1, -1\}$ M_y eigenvalues for $D_z = 0$. A finite D_z splits the degeneracy. Here, we show that the doubly degenerate bands at the X point have M_y eigenvalues $\{+1, +1\}$ or $\{-1, -1\}$ for finite D_z.

The relevant symmetries at the X point are M_y, $\overline{C}_{2y} := t(\mathbf{a}_2)C_{2y}$ (the combination of twofold rotation symmetry and a translation along $\mathbf{a}_2$), and M_x. Here, $\mathbf{a}_1 = (1, 0)$ and $\mathbf{a}_2 = (1/2, \sqrt{3}/2)$ are the lattice vectors of the nonmagnetic unit cell [see Fig. 1(b) in the main text]. We now work out the commutation relation between the symmetry operators,

$$M_x M_y = M_y M_x,$$
$$M_y \overline{C}_{2y} = M_y t(\mathbf{a}_2) C_{2y}$$
$$= t(-\mathbf{a}_2 + \mathbf{a}_1) M_y C_{2y}$$
$$= t(-2\mathbf{a}_2 + \mathbf{a}_1) \overline{C}_{2y} M_y$$
$$= \overline{C}_{2y} M_y,$$
$$M_x \overline{C}_{2y} = M_x t(\mathbf{a}_2) C_{2y}$$
$$= t(-\mathbf{a}_1 + \mathbf{a}_2) M_x C_{2y}$$
$$= t(-\mathbf{a}_1) \overline{C}_{2y} M_x$$
$$= -\overline{C}_{2y} M_x,$$

where we have used the fact that $t(-2\mathbf{a}_2 + \mathbf{a}_1) = 1$ and $t(-\mathbf{a}_1) = -1$ at the X point. We now use proof by contradiction and assume one doubly degenerate band at the X point contains states $\{\varphi_{+1}, \varphi_{-1}\}$ with M_y eigenvalues $\{+1, -1\}$. Since M_x commutes with M_y, $M_x\varphi_{+1}$ should also be an M_y eigenstate with $+1$ eigenvalue. Therefore, $M_x\varphi_{+1} \propto \varphi_{+1}$, which means φ_{+1} is also an eigenstate of M_x with eigenvalue λ. Furthermore, since M_x anticommutes with $\overline{C}_{2y}$, $\overline{C}_{2y}\varphi_{+1}$ should be an eigenstate of M_x with eigenvalue $-\lambda$. As a result, $\overline{C}_{2y}\varphi_{+1} \propto \varphi_{-1}$. Finally, M_y commutes with $\overline{C}_{2y}$, indicating $\overline{C}_{2y}\varphi_{+1} \propto \varphi_{-1}$ is an eigenstate of M_y with eigenvalue $+1$. This contradicts the original assumption that φ_{-1} is an eigenstate of M_y with eigenvalue -1. Therefore, every doubly degenerate band at X has M_y eigenvalues $\{+1, +1\}$ or $\{-1, -1\}$.

[1] M. Z. Hasan and C. L. Kane, Rev. Mod. Phys. **82**, 3045 (2010).

[2] X.-L. Qi and S.-C. Zhang, Rev. Mod. Phys. **83**, 1057 (2011).

[3] F. D. M. Haldane, Rev. Mod. Phys. **89**, 040502 (2017).

[4] Y. Zhang, Y.-W. Tan, H. L. Stormer, and P. Kim, Nature (London) **438**, 201 (2005).

[5] K. S. Novoselov, A. K. Geim, S. V. Morozov, D. Jiang, M. I. Katsnelson, I. V. Grigorieva, S. V. Dubonos, and A. A. Firsov, Nature (London) **438**, 197 (2005).

[6] C.-K. Chiu, J. C. Y. Teo, A. P. Schnyder, and S. Ryu, Rev. Mod. Phys. **88**, 035005 (2016).

[7] N. P. Armitage, E. J. Mele, and A. Vishwanath, Rev. Mod. Phys. **90**, 015001 (2018).

[8] L. Lu, J. D. Joannopoulos, and M. Soljačić, Nat. Photon. **8**, 821 (2014).

[9] T. Ozawa, H. M. Price, A. Amo, N. Goldman, M. Hafezi, L. Lu, M. C. Rechtsman, D. Schuster, J. Simon, O. Zilberberg, and I. Carusotto, Rev. Mod. Phys. **91**, 015006 (2019).

[10] R. Süsstrunk and S. D. Huber, Proc. Natl. Acad. Sci. USA **113**, E4767 (2016).

[11] T. Zhang, Z. Song, A. Alexandradinata, H. Weng, C. Fang, L. Lu, and Z. Fang, Phys. Rev. Lett. **120**, 016401 (2018).

[12] F. Y. Li, Y. D. Li, Y. B. Kim, L. Balents, Y. Yu, and G. Chen, Nat. Commun. **7**, 12691 (2016).

[13] S. S. Pershoguba, S. Banerjee, J. C. Lashley, J. Park, H. Ågren, G. Aeppli, and A. V. Balatsky, Phys. Rev. X **8**, 011010 (2018).

[14] L. Chen, J. H. Chung, B. Gao, T. Chen, M. B. Stone, A. I. Kolesnikov, Q. Huang, and P. Dai, Phys. Rev. X **8**, 041028 (2018).

[15] Z. Cai, S. Bao, Z.-L. Gu, Y.-P. Gao, Z. Ma, Y. Shangguan, W. Si, Z.-Y. Dong, W. Wang, Y. Wu, D. Lin, J. Wang, K. Ran, S. Li, D. Adroja, X. Xi, S.-L. Yu, X. Wu, J.-X. Li, and J. Wen, Phys. Rev. B **104**, L020402 (2021).

[16] L. Chen, J. H. Chung, M. B. Stone, A. I. Kolesnikov, B. Winn, V. O. Garlea, D. L. Abernathy, B. Gao, M. Augustin, E. J. G. Santos, and P. Dai, Phys. Rev. X **11**, 031047 (2021).

[17] F. Zhu, L. Zhang, X. Wang, F. José dos Santos, J. Song, T. Mueller, K. Schmalzl, W. F. Schmidt, A. Ivanov, J. T. Park, J. Xu, J. Ma, S. Lounis, S. Blügel, Y. Mokrousov, Y. Su, and T. Brückel, Sci. Adv. **7**, eabi7532 (2021).

[18] W. Yao, C. Li, L. Wang, S. Xue, Y. Dan, K. Iida, K. Kamazawa, K. Li, C. Fang, and Y. Li, Nat. Phys. **14**, 1011 (2018).

[19] S. Bao, J. Wang, W. Wang, Z. Cai, S. Li, Z. Ma, D. Wang, K. Ran, Z. Y. Dong, D. L. Abernathy, S.-L. Yu, X. Wan, J.-X. Li, and J. Wen, Nat. Commun. **9**, 2591 (2018).

[20] B. Yuan, I. Khait, G. J. Shu, F. C. Chou, M. B. Stone, J. P. Clancy, A. Paramekanti, and Y. J. Kim, Phys. Rev. X **10**, 011062 (2020).

[21] D. Boyko, A. V. Balatsky, and J. T. Haraldsen, Phys. Rev. B **97**, 014433 (2018).

[22] K.-H. Lee, S.-B. Chung, K. Park, and J.-G. Park, Phys. Rev. B **97**, 180401(R) (2018).

[23] A. Y. Kitaev, Ann. Phys. **321**, 2 (2006).

[24] H. Takagi, T. Takayama, G. Jackeli, G. Khaliullin, and S. E. Nagler, Nat. Rev. Phys. **1**, 264 (2019).

[25] H. B. Cao, A. Banerjee, J.-Q. Yan, C. A. Bridges, M. D. Lumsden, D. G. Mandrus, D. A. Tennant, B. C. Chakoumakos, and S. E. Nagler, Phys. Rev. B **93**, 134423 (2016).

[26] J. G. Rau, E. K.-H. Lee, and H.-Y. Kee, Annu. Rev. Condens. Matter Phys. **7**, 195 (2016).

[27] E. A. Zvereva, M. I. Stratan, Y. A. Ovchenkov, V. B. Nalbandyan, J. Y. Lin, E. L. Vavilova, M. F. Iakovleva, M. Abdel-Hafiez, A. V. Silhanek, X. J. Chen, A. Stroppa, S. Picozzi, H. O. Jeschke, R. Valentí, and A. N. Vasiliev, Phys. Rev. B **92**, 144401 (2015).

[28] A. K. Bera, S. M. Yusuf, A. Kumar, and C. Ritter, Phys. Rev. B **95**, 094424 (2017).

[29] E. A. Zvereva, M. I. Stratan, A. V. Ushakov, V. B. Nalbandyan, I. L. Shukaev, A. V. Silhanek, M. Abdel-Hafiez, S. V. Streltsov, and A. N. Vasiliev, Dalton Trans. **45**, 7373 (2016).

[30] F. Ye, S. Chi, H. Cao, B. C. Chakoumakos, J. A. Fernandez-Baca, R. Custelcean, T. F. Qi, O. B. Korneta, and G. Cao, Phys. Rev. B **85**, 180403(R) (2012).

[31] C. Kim, J. Jeong, P. Park, T. Masuda, S. Asai, S. Itoh, H.-S. Kim, A. Wildes, and J.-G. Park, Phys. Rev. B **102**, 184429 (2020).

[32] C. Wong, M. Avdeev, and C. D. Ling, J. Solid State Chem. **243**, 18 (2016).

[33] A. I. Kurbakov, A. N. Korshunov, S. Yu Podchezertsev, M. I. Stratan, G. V. Raganyan, and E. A. Zvereva, J. Alloys Compd. **820**, 153354 (2020).

[34] S. K. Choi, R. Coldea, A. N. Kolmogorov, T. Lancaster, I. I. Mazin, S. J. Blundell, P. G. Radaelli, Y. Singh, P. Gegenwart, K. R. Choi, S.-W. Cheong, P. J. Baker, C. Stock, and J. Taylor, Phys. Rev. Lett. **108**, 127204 (2012).

[35] M. Songvilay, J. Robert, S. Petit, J. A. Rodriguez-Rivera, W. D. Ratcliff, F. Damay, V. Balédent, M. Jiménez-Ruiz, P. Lejay, E. Pachoud, A. Hadj-Azzem, V. Simonet, and C. Stock, Phys. Rev. B **102**, 224429 (2020).

[36] L. P. Regnault, J. Y. Henry, J. Rossat-Mignod, and A. De Combarieu, J. Magn. Magn. Mater. **15-18**, 1021 (1980).

[37] L. P. Regnault, J. Rossat-Mignod, J. Y. Henry, R. Pynn, and D. Petitgrand, in *Magnetic Excitations and Fluctuations*, edited by S. W. Lovesey, U. Balucani, F. Borsa, and V. Tognetti, Springer Series in Solid-State Sciences Vol. 54 (Springer, Berlin, Heidelberg, 1984), pp. 201–206.

[38] L. P. Regnault, J. P. Boucher, J. Rossat-Mignod, J. Bouillot, R. Pynn, J. Y. Henry, and J. P. Renard, Physica B+C **136**, 329 (1986).

[39] L. P. Regnault, J. Rossat-Mignod, J. Y. Henry, and L. J. de Jongh, J. Magn. Magn. Mater. **31-34**, 1205 (1983).

[40] L. P. Regnault and J. Rossat-Mignod, in *Phase Transitions in Quasi Two-Dimensional Planar Magnets*, edited by L. J. De Jongh (Kluwer Academic, Dordrecht, 1990), pp. 271–320.

[41] L.-P. Regnault, C. Boullier, and J. E. Lorenzo, Heliyon **4**, e00507 (2018).

[42] R. Zhong, T. Gao, N. P. Ong, and R. J. Cava, Sci. Adv. **6**, eaay6953 (2020).

[43] J. L. Lado and J. Fernández-Rossier, 2D Mater. **4**, 035002 (2017).

[44] S. Toth and B. Lake, J. Phys.: Condens. Matter **27**, 166002 (2015).

[45] G. Jackeli and G. Khaliullin, Phys. Rev. Lett. **102**, 017205 (2009).

[46] E. S. Klyushina, B. Lake, A. T. M. N. Islam, J. T. Park, A. Schneidewind, T. Guidi, E. A. Goremychkin, B. Klemke, and M. Månsson, Phys. Rev. B **96**, 214428 (2017).

[47] L. W. Harriger, M. Liu, H. Luo, R. A. Ewings, C. D. Frost, T. G. Perring, and P. Dai, Phys. Rev. B **86**, 140403(R) (2012).

[48] P. Dai, Rev. Mod. Phys. **87**, 855 (2015).

[49] J. P. Wicksted, P. Böni, and G. Shirane, Phys. Rev. B **30**, 3655 (1984).

[50] D. L. Abernathy, M. B. Stone, M. J. Loguillo, M. S. Lucas, O. Delaire, X. Tang, J. Y. Y. Lin, and B. Fultz, Rev. Sci. Instrum. **83**, 15114 (2012).

[51] J. B. Fouet, P. Sindzingre, and C. Lhuillier, Eur. Phys. J. B **20**, 241 (2001).

[52] H.-S. Kim and H.-Y. Kee, Phys. Rev. B **93**, 155143 (2016).

[53] L. Wu, A. Little, E. E. Aldape, D. Rees, E. Thewalt, P. Lampen-Kelley, A. Banerjee, C. A. Bridges, J. Q. Yan, D. Boone, S. Patankar, D. Goldhaber-Gordon, D. Mandrus, S. E. Nagler, E. Altman, and J. Orenstein, Phys. Rev. B **98**, 094425 (2018).